

# A core–shell fiber moisture-driven electric generator enabled by synergetic complex coacervation and built-in potential

Received: 1 May 2024

Accepted: 11 November 2024

Published online: 20 November 2024

 Check for updates

Guangtao Zan <sup>1,5</sup>, Wei Jiang<sup>1,5</sup>, HoYeon Kim <sup>1,5</sup>, Kaiying Zhao <sup>1</sup>, Shengyou Li <sup>1</sup>, Kyuho Lee <sup>1</sup>, Jihye Jang<sup>1</sup>, Gwanho Kim<sup>1</sup>, EunAe Shin<sup>1,2</sup>, Woojoong Kim<sup>1</sup>, Jin Woo Oh<sup>1</sup>, Yeonji Kim<sup>1</sup>, Jong Woong Park <sup>1</sup>, Taebin Kim<sup>1</sup>, Seonju Lee<sup>1</sup>, Ji Hye Oh<sup>1</sup>, Jowon Shin<sup>3</sup>, Hyeong Jun Kim <sup>3</sup> & Cheolmin Park <sup>1,4</sup> 

Moisture-driven electricity generators (MEGs) have been extensively researched; however, high-performance flexible variants have seldom been demonstrated. Here we present a novel complex coacervation with built-in potential strategy for developing a high-performance uniaxial MEG, featuring a core of poly(3,4-ethylenedioxythiophene) (PEDOT) with a built-in charge potential and a gel shell composed of poly(diallyldimethylammonium chloride) (PDDA) and sodium alginate (NaAlg) coacervate. The complex coacervation of two oppositely charged polyelectrolytes produces extra mobile carriers and free volume in the device; meanwhile, the PEDOT core's surface charge significantly accelerates carrier diffusion. Consequently, the uniaxial fiber-based MEG demonstrates breakthrough performance, achieving an output voltage of up to 0.8 V, a maximum current density of 1.05 mA/cm<sup>2</sup>, and a power density of 184 μW/cm<sup>2</sup> at 20% relative humidity. Moreover, the mechanical robustness is ensured for the PEDOT nanoribbon substrate without performance degradation even after 100,000 folding cycles, making it suitable for self-powered human interactive sensor and synapse. Notably, we have constructed the inaugural MEG-synapse self-powered device, with a fiber-based MEG successfully operating a synaptic memristor, thereby emulating autonomous human synapses linked with fibrous neurons. Overall, this work pioneers innovative design strategies and application scenarios for high-performance MEGs.

The development of self-powered flexible, wearable electronic devices has drawn considerable attention for advancing human–machine interface technology. Consequently, various sophisticated electric generators capable of harvesting ambient energy, including friction-based/piezoelectric nanogenerators, thermoelectric generators, solar

cells, and moisture-driven electric generators (MEGs), have been devised<sup>1–7</sup>. Among them, MEGs show promise because their operation is based on ubiquitously available moisture, which makes them potentially suitable for self-powered electronics when some requirements are met such as high harvesting performance comparable with other

<sup>1</sup>Department of Materials Science and Engineering, Yonsei University, Seoul, Republic of Korea. <sup>2</sup>Korea Packaging Center, Korea Institute of Industrial Technology, Bucheon, Republic of Korea. <sup>3</sup>Department of Chemical and Biomolecular Engineering, Sogang University, Seoul, Republic of Korea. <sup>4</sup>Post-Silicon Semiconductor Institute, Korea Institute of Science and Technology, Seoul, Republic of Korea. <sup>5</sup>These authors contributed equally: Guangtao Zan, Wei Jiang, HoYeon Kim. ✉ e-mail: [cmpark@yonsei.ac.kr](mailto:cmpark@yonsei.ac.kr)

alternatives, excellent mechanical resilience, breathability, and biocompatibility<sup>8–16</sup>. Although high-performance MEGs have been extensively researched by exploring novel materials with optimized device structures, such as graphene oxides<sup>17–21</sup>, carbon dots<sup>22,23</sup>, hydrogels<sup>24–27</sup>, proteins<sup>1,28,29</sup>, aerogels<sup>30</sup>, and polyelectrolytes<sup>2,31–34</sup>, their energy-harvesting performance remains subpar, thereby necessitating the development of novel material strategies for boosting performance.

Previous studies have shown that the relatively low current density generated from a MEG is responsible for the low power density often arising from the limited number of mobile ions preferentially dissociated on the energy-generating material and their long transport pathways with slow diffusion rates. To address this fundamental challenge in the MEG, we envisioned that complex coacervation involving phase-segregation of two oppositely charged polyelectrolytes driven by enthalpy and entropy, known as one of the most effective microencapsulation techniques extensively used across the pharmaceutical, food, agriculture, and textile industries<sup>35,36</sup>, would be promising because abundant extra mobile ions are readily produced

during the complex coacervation. In addition, the phase segregation associated with the densified coacervation increases the free volume in the system, allowing the fast diffusion of the ions. To further facilitate the diffusion of the ions, a core-shell-structured fiber-based MEG is proposed with a mechanically flexible electrode core and coacervate shell, also making the MEG resilient to diverse mechanical deformations such as bending, folding, rolling, and twisting.

Here we present a complex coacervation with built-in potential strategy for developing a high-performance core-shell-structured fiber-based MEG with mechanical pliability. The core-shell fiber-type MEG comprised a poly(3,4-ethylenedioxythiophene) (PEDOT) core and a coacervate of poly(diallyldimethylammonium chloride) (PDDA) and sodium alginate (NaAlg) as the shell, which was wrapped with a Cu-thread-based outer electrode (Fig. 1a). During entropically driven complex coacervation of oppositely charged PDDA and NaAlg in the fiber shell, abundant mobile counterions are additionally released with newly generated free volume, enabling rapid, facile diffusion of the mobile ions to the Cu electrode. Moreover, the PEDOT core with a

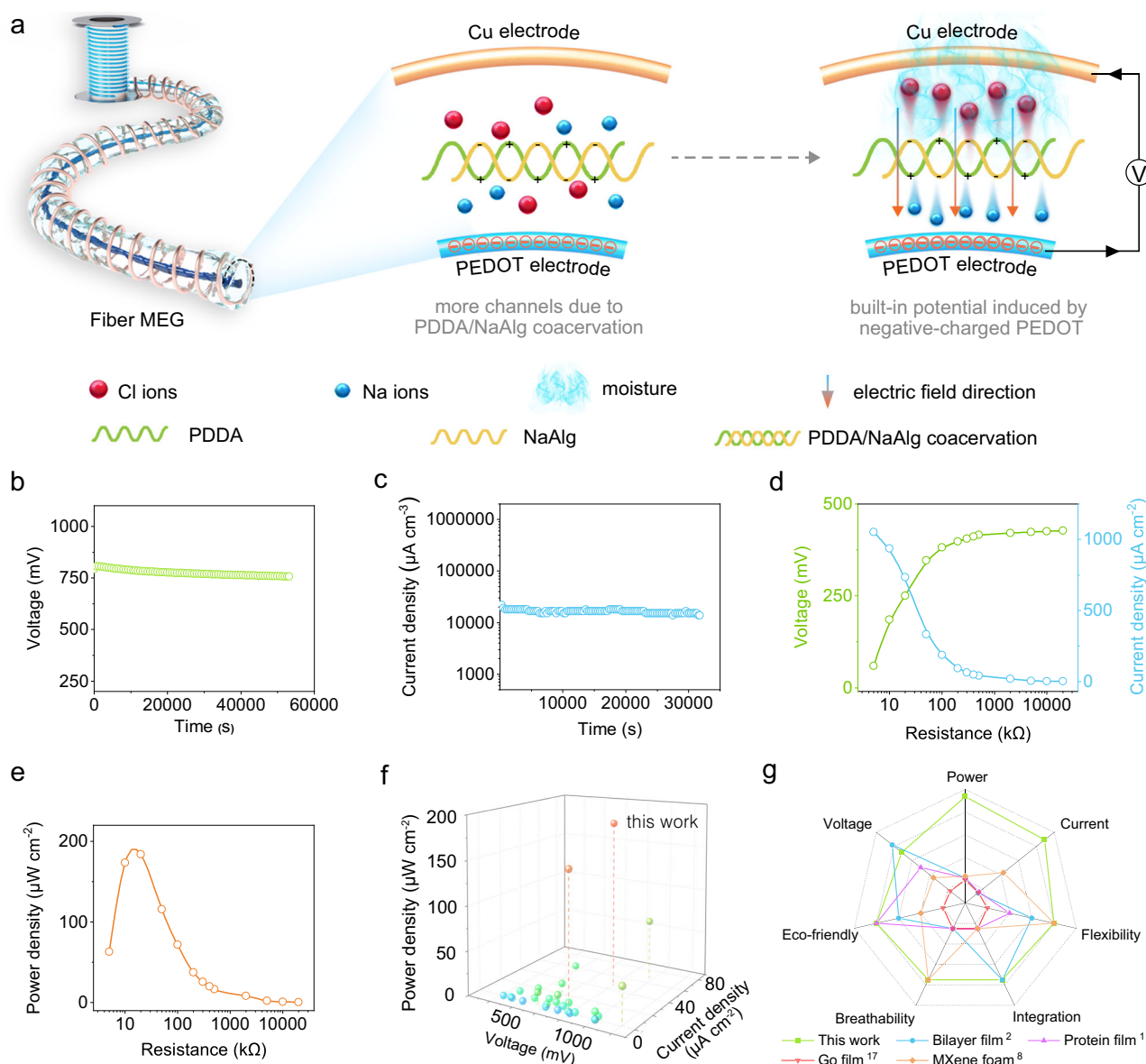


**Fig. 1 | Design and properties of the fiber-based MEG.** **a** Schematic of synergetic strategy of complex coacervation and built-in potential. **b** Output voltage, **c** current density, **d** voltage and current density with variable electrical resistance, and

**e** corresponding power density of the fiber-based MEG at 20% RH. **f** Performances of the fiber-based MEG and previously reported MEGs. **g** Comparative radar chart of representative MEGs.

negative surface potential (built-in potential) facilitates charge separation with field-directional ion diffusion, yielding a high-performance fiber-based MEG with excellent flexibility. Self-powered information transmission was achieved based on the finger-motion interactive MEG. Furthermore, long-term operating artificial synaptic memristor is constructed by connecting our fiber-based MEG to the synapse, emulating autonomous human synapses linked with fibrous neurons.

## Results

### Design and preparation of fiber-based MEG

A high-performance MEG containing fibers with a PEDOT core and PDDA/NaAlg coacervate gel shell (PEDOT@PDDA/NaAlg) enveloped by a Cu wire electrode was fabricated (Fig. 1a). In the device, the polyelectrolyte coacervate gel featuring oppositely charged PDDA and NaAlg was employed as the energy-generating part of the MEG. Therefore, PDDA/NaAlg coacervate can be considered a homogenous electricity-generating material, distinct from the bilayer heterogeneous structure made using two separate polyelectrolytes<sup>2</sup>. The conductive PEDOT nanoribbons with an inherently negative surface electrostatic potential served as the inner electrode, with flexible, thin Cu wire functioning as the outer electrode. The PEDOT electrode could induce a built-in potential when assembled with the Cu metal electrode, thereby generating a driving force to facilitate the directional diffusion of charge carriers, thus improving the MEG performance. Additionally, when PDDA and NaAlg coacervated with each other, numerous mobile ions were released with the increased free volume of the gel arising from the robust polymer–polymer assembly during coacervation<sup>37</sup>. The increased number of free counterions as well as the greater free volume after coacervation led to a higher number of charge carriers and accelerated ion diffusion, effectively enhancing the output performance of the MEG (Fig. 1a). Interestingly, the fiber-based MEG exhibited a remarkable open-circuit voltage of 0.8 V and a short-circuit current density of 1.05 mA/cm<sup>2</sup> under ambient conditions (20% relative humidity (RH) and 25 °C) (Fig. 1b, c). Moreover, the device operated stably for -15 h in continuous mode. Consequently, it outputted a high power density of -178 μW/cm<sup>2</sup> (Fig. 1d, e). This high performance makes it stand out among various reported MEGs under similar conditions (Fig. 1f; Supplementary Tables 1,2).

In addition to the above excellent energy-generating performance, the MEG was conducive to green, sustainable fabrication and exhibited remarkable biocompatibility, flexibility, weavability, integration, and breathability, thereby demonstrating comprehensive advantages compared to the reported MEGs. It should be noted that integral MEG devices that simultaneously combine high mechanical flexibility have rarely been demonstrated, primarily owing to the use of highly conductive yet rigid metals as electrodes and the mandatory sealing of one side in most thin-film MEGs, which significantly limit their flexibility and breathability. The use of flexible electrodes to construct fiber-structured devices effectively addresses the aforementioned issues. The core-shell structure of the fibers forms a self-sealing configuration, exposing only the outer surface to moisture, which creates an ion concentration gradient. The fine electrodes within the fibers significantly enhance the overall flexibility of the device. Although several fiber-type MEGs have been reported, they still face challenges such as intermittent power generation, insufficient performance, and limited flexibility<sup>38–40</sup>. To address these challenges, our approach utilizes a super-flexible conducting polymer fiber, encased within a self-sealing coacervate shell, as the electrode. This design not only ensures mechanical flexibility with soft PEDOT core electrode but also significantly improves output performance due to the synergistic effects of complex coacervation and built-in potential. Additionally, weaving these fibers into a textile enhances breathability, an important feature for practical applications. Furthermore, the biocompatibility is assured by the eco-friendly nature of all components used in our core-shell fibers. As illustrated in the radar chart in Fig. 1g,

we compared our MEGs with several representative MEGs. We plotted the values of voltage, current density, and power density, and also ranked the characteristics of flexibility, eco-friendliness, integration, and breathability, which exhibits the unique comprehensive features of our MEG device.

An optimal device fabrication route based on two-step wet spinning was realized through extensive experimental exploration and condition optimization (Fig. 2). First, highly conductive PEDOT ribbons with negative surface potential were prepared by large-scale continuous wet spinning (Fig. 2a; Supplementary Fig. 1; Supplementary Movie 1). Notably, the concentration and spinning speed of the PEDOT solution significantly affected the conductivity and mechanical strength of the PEDOT ribbons. Specifically, the PEDOT specimen obtained using the optimized spinning solution (concentration, 3.6%; spinning speed, 2 mL/h) exhibited an electrical conductivity of -4000 S/cm, which is among the highest conductivity values of reported fiber-type PEDOT materials (Supplementary Figs. 2, 3). Structural characterization indicated that the PEDOT sample had a unique ribbon morphology, with a width of -100 μm and thickness of -2 μm (Fig. 2b; Supplementary Figs. 4, 5). Notably, the PEDOT ribbon showed topological grooves on its surface, which presumably helped disperse mechanical stress during deformation (Fig. 2b). Several mechanical tests of the PEDOT ribbons showcased their excellent flexibility. The PEDOT ribbon core withstood bending, folding, curling, and twisting at different angles without structural fracture (Fig. 2c, d; Supplementary Figs. 6, 7). Additionally, no structural damage or conductivity decline occurred when the PEDOT ribbons were folded over 100,000 times, making them ideal electrodes for flexible integral MEGs because they exhibited both high electrical conductivity and exceptional flexibility (Fig. 2f, Supplementary Fig. 8). Moreover, the PEDOT ribbons were hydrophilic (water contact angle, 36°), thereby permitting favorable surface interactions with the coacervate PDDA/NaAlg gel (Fig. 2e).

Subsequently, the PEDOT@PDDA/NaAlg fibers were continuously produced by sequentially immersing the PEDOT ribbons in a 20% CaCl<sub>2</sub> solution and a PDDA/NaAlg mixture with an optimized ratio of 5:20, which was estimated based on the properties of the MEG. Cross-sectional analysis of the resulting coacervate gel fiber revealed a cylindrical structure with an average diameter of 200 μm (Fig. 2g; Supplementary Fig. 9). Energy-dispersive X-ray spectroscopy (EDS) mapping revealed the dominant distribution of PEDOT-derived S in the core (Supplementary Figs. 10, 11) and the uniform distribution of PDDA-derived N in the fiber shell. Furthermore, the mapping results indicated that Na ions were more distributed in the outer regions of the shell. This Na concentration gradient in the shell was likely formed spontaneously during synthesis and helped accelerate ion diffusion and improve the MEG performance (Fig. 2h; Supplementary Fig. 12; Supplementary Table 3). These results validated the preparation of both the PEDOT ribbon core and coacervate gel shell by two-step continuous, rapid mass production.

Various characterization experiments were conducted to investigate the PDDA–NaAlg interactions. Fourier-transform infrared (FT-IR) spectroscopy showed that after the addition of PDDA, the absorbance at 1600 cm<sup>-1</sup>—arising from the stretching of carbonyl in NaAlg—was blue-shifted in all the PEDOT@PDDA/NaAlg fibers, indicating electrostatic interactions between the carboxyl groups in NaAlg and the quaternary ammonium group in PDDA (Fig. 2i; Supplementary Fig. 13). Furthermore, the C=O and C–N peaks of the coacervation products in the high-resolution C1s X-ray photoelectron spectroscopy (XPS) profiles were red shifted, and the quaternary ammonium nitrogen peaks in the high-resolution N1s spectra demonstrated a blue shift, relative to pure NaAlg and pure PDDA (Fig. 2j, k). This suggested that coacervation predominantly occurred between the carboxyl groups in NaAlg and the quaternary ammonium group in PDDA.

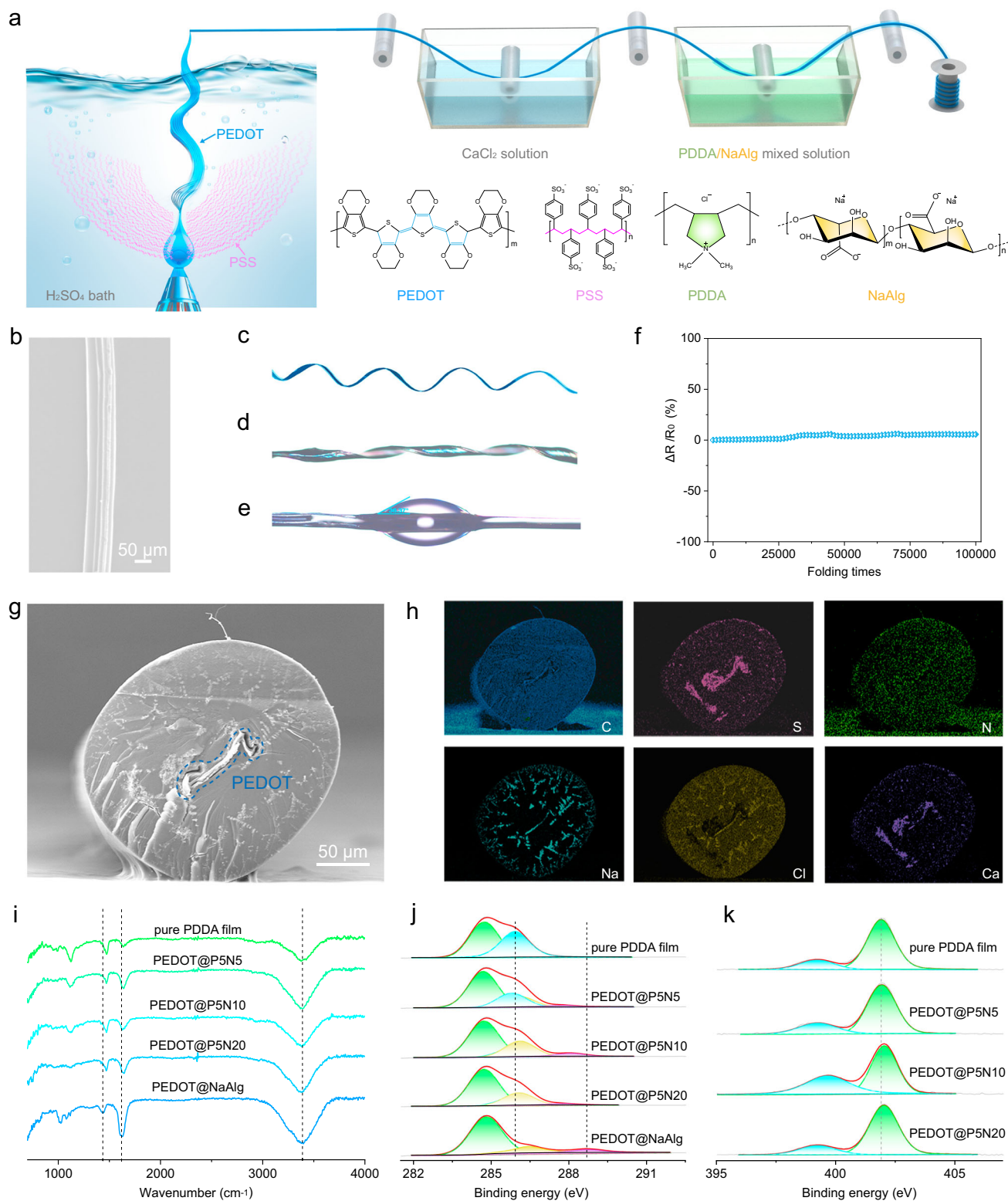


**Fig. 2 | Preparation and structures of the PEDOT@PDDA/NaAlg core-shell fiber.** **a** Schematic of preparation. **b** SEM image of PEDOT ribbon. **c** Crimping, **d** twisting, **e** hydrophilicity, and **f** cyclic folding of PEDOT ribbon.

**g, h** Cross section of PEDOT@P5N20 core-shell fiber and corresponding EDS maps. **i** FT-IR spectra, **j** high-resolution C 1s, and **k** high-resolution N 1s XPS profiles of PEDOT-core-based fibers and PDDA film.

Concurrently, the electrostatic interactions between these groups altered the chemical environments of Ca and Cl, leading to significant shifts in the 2p peaks of both Ca and Cl (Supplementary Figs. 14, 15). These results corroborated the complex coacervation of PDDA and NaAlg within fiber.

#### Conditional experiments for MEG performance optimization

The effects of the coacervate gel structures and test conditions on the performance of the MEG were comprehensively investigated (Fig. 3), starting with the influence of the PDDA/NaAlg ratio. Gelation experiments indicated that the mixture rarely precipitated when the NaAlg/

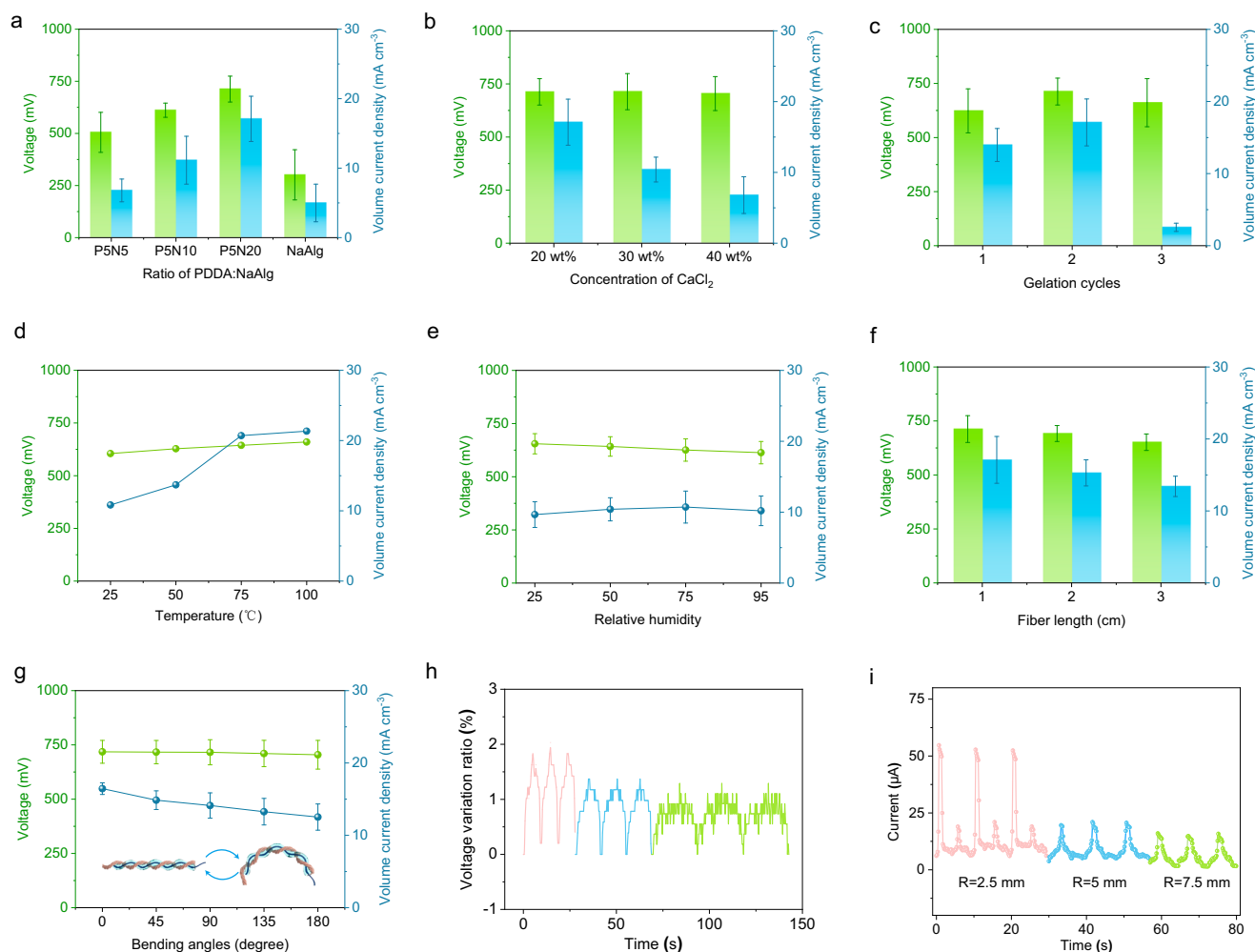


**Fig. 3 | Conditional experiments for performance enhancement of fiber-type MEG.** Properties of (a) fiber-type MEGs with different PDDA/NaAlg ratios at 20% RH, b PEDOT@P5N20 fibers gelated with CaCl<sub>2</sub> at different concentrations, c PEDOT@P5N20 fibers over different gelation cycles, d PEDOT@P5N20 fibers at different temperatures, e, PEDOT@P5N20 fibers at different RH values, and

f PEDOT@P5N20 fibers with different lengths. g Properties of flexible MEG for different bending angles. Real-time variations in (h), voltage and (i) current of the MEG for different (h), bending rates and (i) bending radii. Error bars show standard deviation of recorded data.

PDDA volume ratio was less than 4. Notably, the PDDA/NaAlg coacervate gel was prepared by incorporating Ca ions into the mixed solution (Supplementary Figs. 16, 17; Supplementary Table 4). Notably, the MEG with pure NaAlg generated a voltage of 300 mV and current density of 5 mA/cm<sup>3</sup>. Similarly, pure PDDA produced a voltage of 200 mV and much smaller current density (Supplementary Fig. 18). However, both the output voltage and current substantially increased upon the formation of the coacervate gel. With increasing NaAlg content, the average output voltage escalated from 500 to 750 mV, whereas the volume current density increased from 7 to 17 mA/cm<sup>3</sup> at 20% RH and 25 °C (Fig. 3a). Additionally, the coacervate gel was varied by modifying the charging proportions of NaAlg and PDDA, with optimal MEG performance achieved at a ratio of 5:20. Subsequently, the influence of the CaCl<sub>2</sub> concentration on gelation was assessed, with optimal behavior observed at 20 wt% (Fig. 3b). The low gelation rate realized at low CaCl<sub>2</sub> concentrations potentially favored the MEG performance owing to the uniform pores induced during gelation. Moreover, the effects of the number of gelation cycles on the coacervate gel fiber preparation were explored (Fig. 3c). The MEG showed optimal performance over two gelation cycles, which likely produced a thickness suitable for gradient electricity generation (Supplementary Fig. 19). Additionally, the properties of fibers with different lengths were tested; similar voltages were produced while the current

increased in proportion with the length, laying the foundation for large-scale application of the fiber-type MEG (Fig. 3f).

Additionally, the impacts of test conditions, including temperature and RH, on MEG performance were explored. The device operated reliably and exhibited slightly improved performance as the temperature increased from 25 to 100 °C (Fig. 3d); its working temperature range is very wide compared to reported values. Furthermore, the output voltage and current exhibited only slight increments with increasing RH (Fig. 3e), presumably owing to the excellent hydrophilicity and water retention properties of the fibers (Supplementary Figs. 20–22). At low RH levels, the coacervate gel fibers had already absorbed sufficient moisture for ion dissociation and diffusion. Consequently, a further increase in RH did not significantly enhance the MEG performance. Overall, the wide operating temperature, and stable operation under RH windows, and high power density under low RH of the MEG endow it with the capability to function in the majority of Earth's regions (Supplementary Fig. 23).

Flexibility of both materials and devices is essential for developing advanced flexible, wearable technologies. Subsequently, the properties of the MEG were investigated under different deformation modes (Fig. 3g–i; Supplementary Figs. 24, 25). Initially, the bending and folding capabilities of the fiber-type MEG were characterized for different angles and repetitions manually. As the bending angle was varied, the voltage

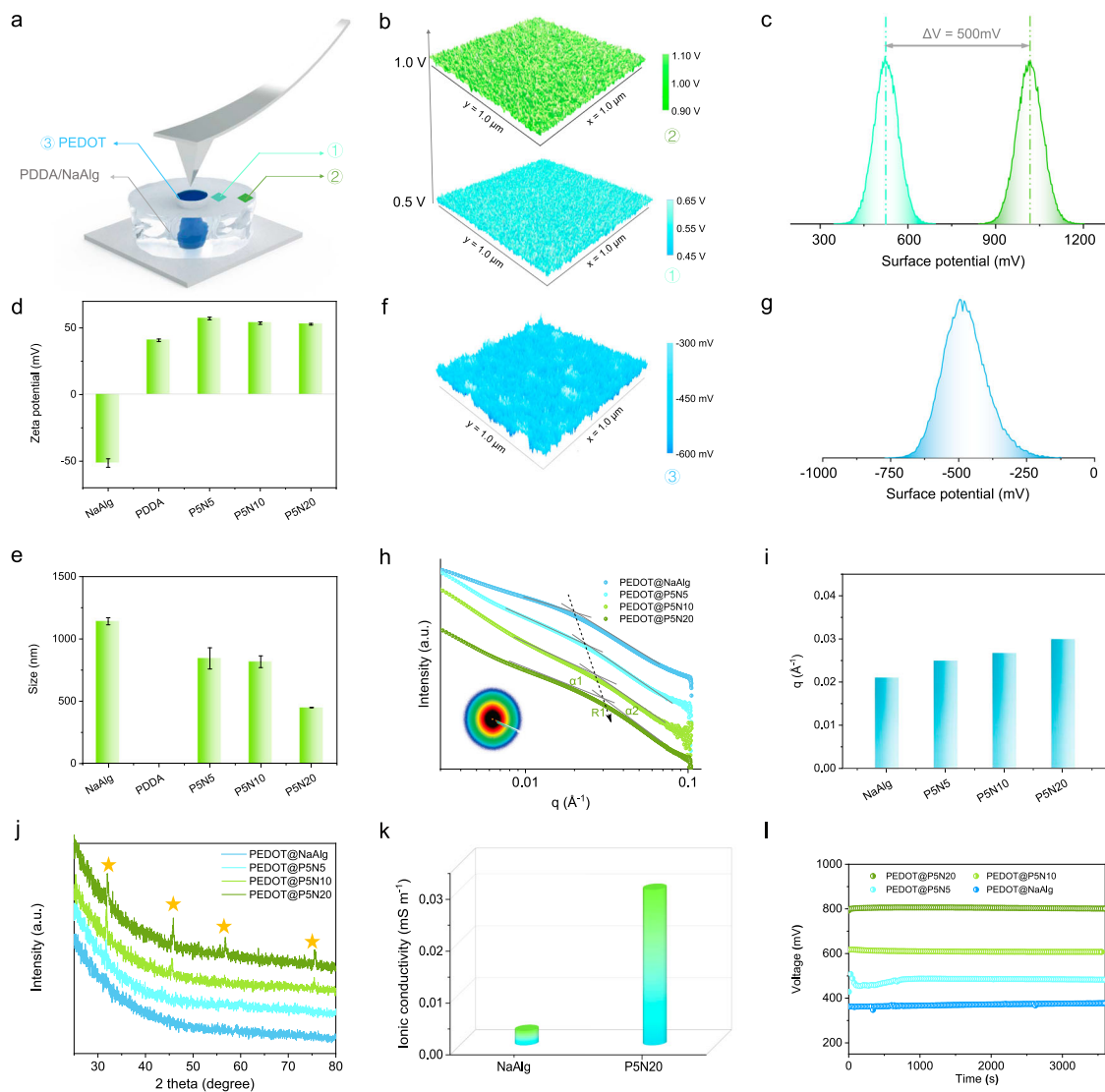


**Fig. 4 | Mechanism underlying MEG operation.** **a** Schematic of the KPFM measurement apparatus. **b, c** KPFM images and corresponding histograms of the two regions shown in **(a)**. **d, e** Zeta potentials and particle sizes of PDDA/NaAlg mixtures with different ratios. **f, g** KPFM image and corresponding histogram of pure PEDOT ribbon. **h, i** Log–log SAXS profiles of PDDA/NaAlg coacervate gel fibers with

different ratios and corresponding  $R$  values (inset of **h**: a representative 2D SAXS pattern). **j** XRD patterns of fibers with different PDDA/NaAlg ratios. **k** Ionic conductivities of pure NaAlg and P5N20 coacervate gels. **l** MEG-associated properties of fiber-type MEGs with different PDDA/NaAlg ratios.

remained relatively stable, and the current diminished slightly at stable states (Fig. 3g–i). This could be due to the variations in the coacervate gel resistance and the contact area between the external electrodes and coacervate gel during deformation. In addition to the aforementioned manual static tests, dynamic bending studies were conducted on the fiber-type MEG to monitor its electrical signal changes in real-time. An analysis of the output voltage variation revealed a noticeable peak with bending, which returned to the initial value once the MEG reverted to its flat state. The voltage variation of the MEG with a change in the bending frequency was only  $\sim 2\%$ . Moreover, the rate of change in current increased significantly with increasing bending frequency. These results collectively underscore the excellent resolution and recognition capabilities of the fiber-type MEG in exhibiting dynamic bending, emphasizing its potential for use in self-powered human–machine interactive domains, as demonstrated later.

### Mechanisms of fiber-type MEG operation

The mechanisms underlying the exceptional performance of the MEG were explored through in-depth experiments and simulations. Kelvin

probe force microscopy (KPFM) revealed a large surface potential difference (up to 500 mV) between specific zones in the core and shell regions of the coacervate gel fiber in an ambient environment (Fig. 4a–c). This ion dissociation and heterogeneous charge distribution along the radial direction were mainly responsible for the electricity-generating ability of the fabricated device. An analysis of the zeta potential, which reflects the surface potential and surface-charge capacity achieved through water adsorption and ion dissociation (Fig. 4d), suggested that pure NaAlg and PDDA possessed negative and positive charges on their surfaces, respectively. Upon coacervation of NaAlg and PDDA, the formed gel exhibited a positive surface charge. Interestingly, the absolute value of the zeta potential after mixing the two components was higher than that of the individual components, thereby enhancing the MEG performance<sup>41</sup>. With the addition of PDDA, the particle size of the PDDA/NaAlg mixtures, which was measured using a zeta potential and particle size analyzer, decreased from 1100 to 450 nm and reached a minimum of 450 nm for P5N20 (Fig. 4e). These results indicated that the tight aggregation of the two polymer chains in P5N20 likely created more free space for facilitating ion

diffusion, as substantiated by the experiments and simulations described below.

Additional investigations were conducted to identify the source of the noteworthy MEG performance, such as the PEDOT electrode. KPFM testing revealed that the surface potential of PEDOT was significantly negative ( $\sim -400$  mV); this behavior differs markedly from that of traditional metallic materials (Fig. 4f, g). This characteristic likely enabled the MEG to generate a built-in electric field along the radial direction, potentially accelerating the ion migration. Various metallic fibers were also employed as substitutes for the PEDOT core electrode, and their MEG-associated performance was assessed. Cyclic voltammetry (CV) technique was used to test the CV curves of the fiber MEG. The CV curves did not show obvious redox peaks, indicating that electrochemical reactions contribute negligibly to the performance. Additionally, we conducted surface observations and elemental analysis of both a pure Cu wire and a Cu wire from a functioning MEG device that had been exposed to 20%RH for 24 h. The results showed that the elemental composition of the two samples remained nearly unchanged, indicating that under the working conditions of our device, the contribution of the Cu wire as a current collector to the MEG is negligible. These results demonstrate that PEDOT significantly boosted both the output voltage and current of the MEG, affirming its unique and critical role in enhancing performance through improved electron and ion transport processes (Supplementary Figs. 26–29). We also used a film system to study the MEG performance of PDDA/NaAlg with symmetric Ag electrodes or PEDOT electrodes, two relatively inert electrodes with high work function. The results showed that with different symmetric inert electrodes, the MEG device's output performance varied: the MEG using symmetric Ag electrodes showed an open-circuit voltage of about 102 mV and a short-circuit current density of  $0.2 \mu\text{A}/\text{cm}^2$ ; while the MEG using symmetric PEDOT electrodes achieved 350 mV and  $20 \mu\text{A}/\text{cm}^2$  (Supplementary Fig. 30). Those results are not the same with using symmetric Cu electrodes. The phenomenon of performance variation when changing electrode pairs has also been reported in other literature as well. That may be related to the inherent work function, surface roughness, and defects of the electrode materials, which affect the formation of the electric double layer on the material surface.

Furthermore, the NaAlg–PDDA interactions were extensively investigated to probe their role in enhancing MEG performance. Small-angle X-ray scattering (SAXS) analysis was conducted to characterize the coacervation structures (Fig. 4h, i; Supplementary Fig. 31). Three important parameters— $\alpha 2$ , RI, and  $\alpha 1$ —have been presented in the log–log SAXS profiles of NaAlg-based materials<sup>42</sup>; they represent the compactness of the rods, size of the rods, and the fractal dimension of the rod network, respectively. The results showed that  $\alpha 2$  increased and RI decreased with increasing NaAlg proportion, indicating a smaller rod size, further confirming the post-coacervation volume contraction. An increase in  $\alpha 1$  signifies the presence of more branched structures in the coacervate gel network, which may generate more micropores and thus promote charge-carrier diffusion. Subsequently, coacervate gel fibers with varying NaAlg/PDDA ratios were prepared, and their MEG-related performances were compared. The results showed that the coacervate gels significantly outperformed pure NaAlg, with the P5N20 variant achieving an impressive maximum output voltage of 0.8 V. These findings underscore the importance of the NaAlg–PDDAs interactions in augmenting MEG efficiency.

The effects of complex coacervation on free ions in the system were tested through X-ray diffractometry (XRD) and ionic conductivity analysis. The XRD patterns showed no obvious peaks for any of the samples with different PDDA/NaAlg ratios, indicating the presence of amorphous structures (Fig. 4j). These structures suggested the existence of abundant ion-diffusion-facilitating internal defects. Notably, peaks of NaCl crystals appeared in the profiles of all coacervate gels, and the intensity slightly increased with the addition of NaAlg; no such

peaks were exhibited by pure NaAlg. These results suggested that complex coacervation released more free ions (Na and Cl) in the gel, plausibly leading to enhanced MEG performance upon moisture absorption. The electrical conductivity tests suggested that the ionic conductivity of P5N20, which exhibited optimal MEG performance, was tenfold that of pure NaAlg, indicating significantly faster ion diffusion (Fig. 4k). The multiple beneficial effects of complex coacervation bestowed on the MEG were validated by comparing the MEG-associated performances of coacervate gel fibers with varying NaAlg/PDDA ratios (Fig. 4l). The results indicated that the composite coacervate gels considerably outperformed pure NaAlg, with the P5N20 variant achieving the maximum output voltage and current (Fig. 4l). These findings highlight the significance of the NaAlg–PDDA interactions in augmenting the MEG efficiency.

Combining all the characterization results, the mechanism behind the performance enhancement is well elucidated. When the fiber MEG absorbs moisture from the air, the complex coacervation of PDDA and NaAlg on the fiber's outer surface begins to dissociate under the influence of water molecules, releasing a large number of freely mobile  $\text{Na}^+$  and  $\text{Cl}^-$  ions as charge carriers. Simultaneously, the PDDA/NaAlg coacervation creates numerous pores that facilitate ion diffusion. Consequently, an ion and water concentration gradient forms radially within the fiber<sup>43,44</sup>. Due to the negatively charged surface of PEDOT, a built-in potential is established between the electrodes when an external circuit is completed, accelerating the inward diffusion of  $\text{Na}^+$  ions from the outer surface along the radial direction, while  $\text{Cl}^-$  ions diffuse in the opposite direction. Therefore, under the synergistic effects of the complex coacervation of the two polyelectrolytes and the built-in potential of the electrodes, the moisture-driven electric generation performance is significantly enhanced.

### Molecular dynamics simulations

Simulations were conducted to further explore the NaAlg–PDDA interactions (Fig. 5). Initially, density functional theory (DFT) calculations were performed to determine the surface potentials of the units within the two polyelectrolytes (Fig. 5a, b). The results indicated that the  $-\text{COOH}$  region in NaAlg and the quaternary ammonium salt zone in PDDA exhibited the highest surface potentials, pinpointing the probable coacervation sites. Molecular dynamics simulations (see “Methods”) were subsequently conducted to investigate the polymer chain interactions in both pure NaAlg and the PDDA/NaAlg system. Their equilibrium structures (Fig. 5e, f) clearly indicated that the PDDA/NaAlg system possessed more free space than that in pure NaAlg. This observation was corroborated in a more three-dimensional manner by videography (Supplementary Movies 2 and 3). The typical post-interaction assembled structure within the PDDA/NaAlg system exhibited a DNA-like double helical structure, which starkly contrasted with the irregular polymer chain segments in pure NaAlg and pure PDDA (Fig. 5c, d). To demonstrate the free volume more vividly, the free volume and polymer chain distribution areas were mapped out through simulations (Fig. 5h, i). The PDDA/NaAlg system contained more blue regions than those in pure NaAlg, indicative of larger pore areas, which is consistent with the SAXS results. The distributions of voids, free volume fractions, and the mean square displacement (MSD) of ions were quantitatively analyzed for both systems to conduct a more comprehensive comparison (Fig. 5g, j, k). The results revealed a broad distribution of voids in the PDDA/NaAlg system, with a greater prevalence of larger gaps (Fig. 5g). Statistical analysis of free space indicated that the free volume fraction of the PDDA/NaAlg system (40%) was significantly higher than that of NaAlg (26%; Fig. 5j). MSD analysis quantified the deviation of the particle position over time relative to a reference position; this is a common measure of the spatial extent in random motion and can be regarded as a measure of the portion of a system “explored” by a random walker. The statistical outcomes indicated that within a mere 5000 fs, the MSD of the PDDA/

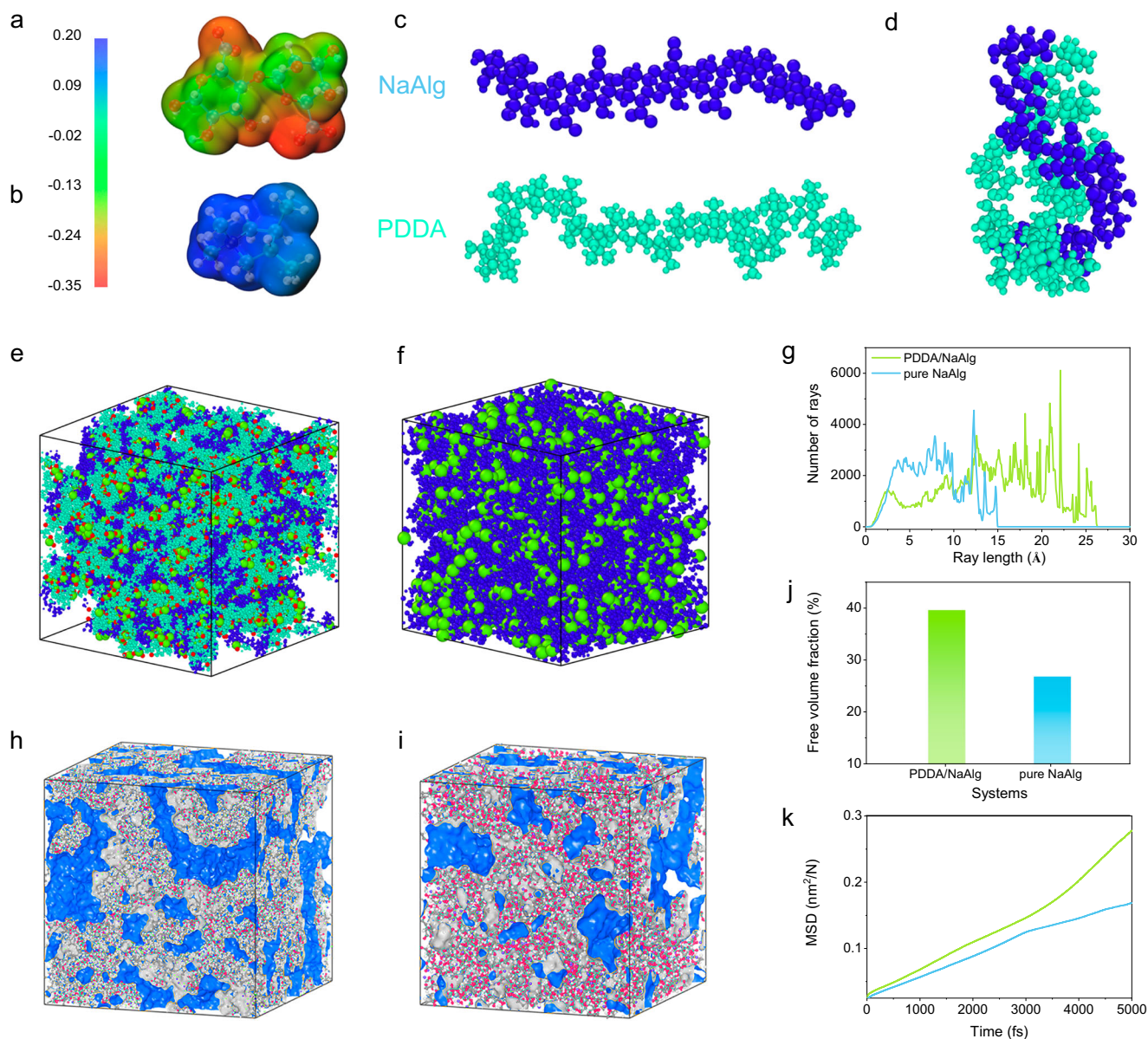


**Fig. 5 | Molecular dynamic simulations.** **a, b** Surface electrostatic potential distributions of NaAlg and PDDA monomers. **c, d** Molecular structures of pure NaAlg, pure PDDA, and PDDA/NaAlg complex (blue chains represent NaAlg and cyan chains represent PDDA). Equilibrium structures of PDDA/NaAlg system (**e**) and pure NaAlg (**f**). **g** Simulated pore size distributions in the equilibrium structures shown in

(**e**) and (**f**). **h, i** Visualization of free volume in the PDDA/NaAlg and pure NaAlg systems (blue and gray zones represent the pore and polymer chain domains, respectively). Free volume fractions (**j**) and mean square displacements (**k**) of the PDDA/NaAlg and pure NaAlg systems.

NaAlg system rapidly increased to 1.65 times that of pure NaAlg. Furthermore, the disparity tended to widen further, indicating that the random ionic motion or diffusion was significantly faster in the PDDA/NaAlg system. This result is consistent with the ion conductivity test findings, indicating a faster ion diffusion rate within the complex coacervation. All the simulation results are consistent with the experimental findings, further certifying that the coacervation of NaAlg and PDDA resulted in the contraction of the polymer backbone and formation of more channels, thereby facilitating ion diffusion and yielding high-performance MEG.

To further validate the efficacy and correctness of the complex coacervation with built-in potential strategy, another coacervate gel featuring PEI and PSS films was constructed; the components were integrated with a PEDOT film and a perforated Cu foil electrode to form an MEG (Supplementary Figs. 32, 33). The MEG tests revealed a substantial enhancement in both voltage and current for the PEI/PSS

coacervate gel film over the pure PEI and PSS films. Specifically, a 100% increase in voltage was observed, with current levels also experiencing a dramatic increase (10× and 100,000×, respectively). Subsequently, replacing the PEDOT film electrode with an Au film yielded an MEG that underperformed its PEDOT-based counterpart, with voltage and current further decreasing by a factor of two and ten, respectively. The above experimental results confirm the effectiveness and versatility of the synergistic complex coacervation and built-in potential strategy in both fiber and film devices.

### Self-powered information exchange

The fiber-based MEG was employed as a self-powered finger motion sensor to enable information encoding by utilizing its exceptional flexibility and dynamic bending resolution. The sensor design was inspired by the traditional telegraph system (Fig. 6a). The classic Morse telegraph relied on an operator manipulating a key to control the

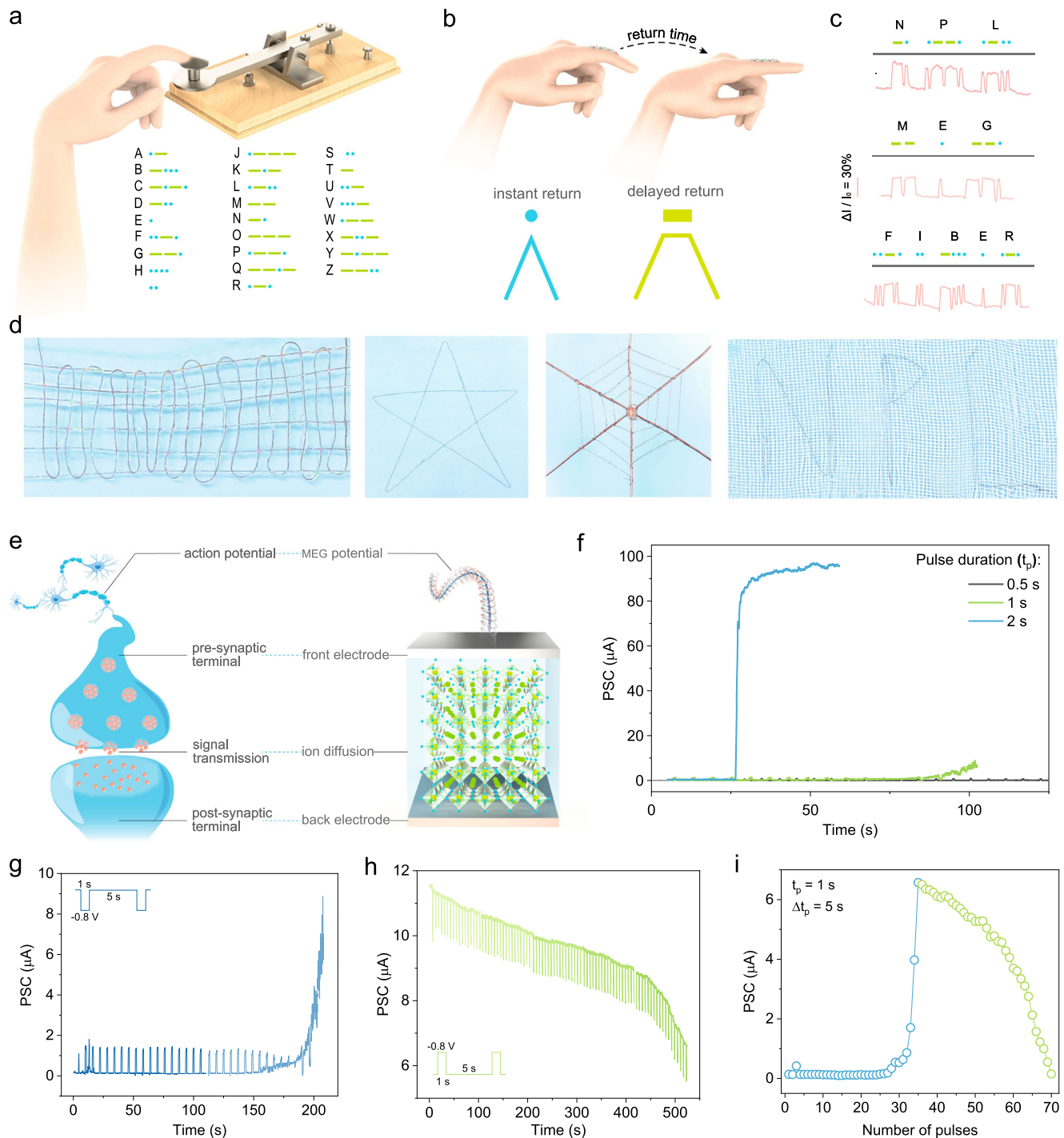


**Fig. 6 | Self-powered device demonstration.** **a** Traditional Morse telegraph model and code. **b** Working principle of the fiber-type MEG-based information transmission device. **c** Information transmission through Morse code using variations of current signals generated by the fiber-type MEG. **d** Integration of fibers into differently shaped systems: a knit fabric, pentagram shape, spiderweb design, and fibers with embedded “NPL” wording incorporated into yarn cloth. **e** Schematics of

an action-potential-induced biological synapse and MEG-potential-powered artificial synaptic device. **f** Long-term potentiation (LTP) curves acquired at different pulse durations using one MEG unit. **g, h** LTP and long-term depression (LTD) curves obtained using one MEG unit. **i**, LTP and LTD plotted against the number of pulses powered by one MEG unit.

interruption of an electrical circuit, thus generating a combination of electrical signals to represent various characters and numbers. The production of dots and dashes through key control constituted the fundamental mechanism of its operation. Inspired by this scheme, the fiber MEG device was designed to be worn on the finger and thereby create similar dots and dashes by controlling the duration for which the finger remained bent. A quick return to a straight position after

bending generated a spike in electrical signals, which represented a dot, whereas a delayed return resulted in a plateaued peak, intuitively signifying a dash (Fig. 6b). In our device, we use changes in current as signals for information transmission. This is because bending causes deformation, which alters the resistance of the shell and the contact area with the electrode, resulting in noticeable variations in current. Using this principle, information was transmitted by detecting the

electrical signals produced during finger bending. The fiber-based MEG device clearly transmitted information in the form of words such as NPL, Fiber, and MEG (Fig. 6c). The corresponding peaks had distinct, easily discernible shapes. More importantly, the device did not require an external power source, as it could operate using the electrical energy harvested from moisture in the air. This showcases the vast potential of the device for use in the advanced domain of self-powered information exchange.

The above results affirm the exceptional flexibility of the single fibers; however, their further assembly and integration are crucial for practical applications. Manual assembly experiments indicated that the coacervate gel fibers could be woven into various structures or shapes, such as fabrics, pentagrams, and spiderwebs (Fig. 6d). Moreover, they were embedded into cloth to form different patterns and underwent various reversible deformations. These findings conclusively demonstrate the impressive assembly and integration capabilities of the coacervate gel fibers, laying the groundwork for their large-scale applications. In summary, the fibrous MEG device exhibits significantly greater post-assembly flexibility than that of previously reported film-like and 3D structures, owing to the use of flexible electrodes. Moreover, the woven structure introduces numerous mesh openings, imparting unparalleled breathability to the device, which is a distinctive advantage of wearable devices.

### Self-powered synaptic device

To further leverage the long-term operational features of the self-powered fiber-based MEG, the device was employed to power an artificial synaptic device by mimicking the action potential of a synapse under ambient conditions (Fig. 6e). In biological synapses, action potentials originating from presynaptic neurons are transferred to the synaptic cleft through presynaptic neuron axons, and neurotransmitters are released from the synaptic vesicle into the synaptic cleft, where they are received by postsynaptic membrane receptors to generate a postsynaptic current (PSC). The PSC amplitude can be determined by the synaptic weight ( $w$ ) between the pre- and postsynaptic neurons, which facilitates the potentiation or depression of the synapse, depending on the charged ions diffusing into the dendrite plasma membrane. In our device, the fiber MEG potential could act as the action potential for driving the synaptic device, with the hole carriers in the perovskite functioning as neurotransmitters and Ag and indium tin oxide (ITO) electrodes used to collect current signals like two terminals in the biological synapse. Therefore, the combination of the above components helped form the first self-powered MEG-driven artificial synaptic device. Diverse tests were conducted to evaluate the working conditions of the self-powered synapse. First, the influence of pulse duration on the PSC, which was controlled by a relay connected to the circuit, was explored. The results indicated that one MEG unit was sufficient for powering the synaptic device at a pulse duration of 0.5 s. Notably, the device achieved a higher PSC over a shorter period with increasing pulse duration (Fig. 6f). The long-term neuroplasticity of the device was investigated at a pulse duration of 0.5 s; this included analyses of the long-term potentiation (LTP) and long-term depression (LTD), which are the primary mechanisms governing learning and memory storage in the human brain. The device showed good neuroplasticity at high pulse numbers, and the growth rate of the PSC was relatively low, emphasizing its potential for certain accurate applications (Fig. 6g–i). Overall, these results underline the prospects of the fabricated MEG for long-term self-powered device operation, given the successful fabrication of the first combined MEG–synapse self-powered device, to our knowledge.

### Discussion

This study demonstrated a significant advancement in the field of MEGs by implementing a synergetic complex coacervation and built-in potential strategy and developing a unique PEDOT@PDDA/NaAlg

core–shell coacervate gel fiber. The PEDOT@PDDA/NaAlg coacervate gel fiber exhibited remarkable performance characteristics, including an output voltage of up to 0.8 V, current density of 1.05 mA/cm<sup>2</sup>, and power density of 184  $\mu$ W/cm<sup>2</sup> at 20% RH, along with addressing the challenges of achieving high flexibility. The mechanism underlying the performance enhancement was elucidated, with the coacervation of oppositely charged PDDA and NaAlg polyelectrolytes within the fiber shell resulting in the release of abundant counterions as charge carriers in addition to the creation of large ion-diffusion channels. Moreover, the negative surface potential of the conductive PEDOT core of the fiber MEG facilitated charge-carrier diffusion, enhancing the MEG performance. Owing to the excellent flexibility and weavability of the PEDOT@PDDA/NaAlg fibers, the fiber-based MEG was successfully employed in a self-powered information exchange device as well as an artificial synapse device. Given its tremendous potential in flexible power generation and human–machine interactions, the PEDOT@PDDA/NaAlg coacervate gel fiber shows promise for advanced applications in various fields.

### Methods

#### Materials

NaAlg, PDDA, calcium chloride, concentrated sulfuric acid, ethanol, and deionized water were purchased from Sigma-Aldrich. An aqueous PEDOT:PSS dispersion (Clevios™ PH 1000; concentration, ~1.2%) was obtained from Heraeus Epurio.

#### Preparation of PEDOT ribbons

The spinning formulation comprised a 3.6 wt% PEDOT:PSS solution, which was prepared by removing a portion of water from the original commercial product at 60 °C. Prior to wet spinning, the spinning formulation was ultrasonicated for 30 min to eliminate bubbles. The ribbons were prepared using a self-constructed wet-spinning system at room temperature (Fig. 2a). The process involved loading the spinning formulation into a 6 mL syringe, which was then connected to a micro-injection pump. The formulation was extruded into a concentrated H<sub>2</sub>SO<sub>4</sub> coagulation bath through a 23 G blunt needle positioned at the bottom, at a spinning flow rate of 2 mL/h. The resulting product—that is, the PEDOT ribbons—was passed through a washing bath containing a 3:1 ethanol/water mixture (by volume) to remove any residual H<sub>2</sub>SO<sub>4</sub>. The PEDOT ribbons were then dried and wound onto a spool.

#### Preparation of PEDOT@PDDA/NaAlg coacervate gel fibers

The typical procedure adopted to fabricate coaxial PEDOT@PDDA/NaAlg coacervate gel fibers is described henceforth: First, a 1 wt% aqueous NaAlg solution was prepared, and different volumes of this solution were mixed with a 35 wt% aqueous PDDA solution to form precursor mixtures for coacervate gel formation; the mixing ratio is denoted as P<sub>x</sub>N<sub>y</sub>, where  $x$  and  $y$  represent the volumes of PDDA and NaAlg, respectively. Next, the ribbons were sequentially immersed in a 20 wt% CaCl<sub>2</sub> solution, the P<sub>x</sub>N<sub>y</sub> coacervate gel precursor solution, and a 20 wt% CaCl<sub>2</sub> solution, to facilitate the formation of the outer coacervate gel layer through ion-induced gelation. Subsequently, coaxial PEDOT@P<sub>x</sub>S<sub>y</sub> coacervate gel fibers were obtained and dried under ambient conditions. The coacervate gel fibers were wrapped with thin Cu wires to assemble super-flexible fiber-based MEG devices for further tests.

#### Characterization methods

Morphologies and microstructures were examined by field-emission scanning electron microscopy (FE-SEM; JEOL, 7001F). The elemental compositions and distributions of the samples were analyzed using an EDS unit attached to the FE-SEM instrument. The chemical elements and their binding states were investigated by XPS using a K-Alpha spectroscope (Thermo Scientific, USA). The crystal structures of the samples were explored by XRD using a Bruker D8 Focus diffractometer

with Cu K $\alpha$  radiation ( $\lambda = 0.15418$  nm) at 40 kV and 40 mA. FT-IR spectra were acquired using a Bruker VERTEX 70 FT-IR spectrometer. SAXS data were collected using the PLS-II 9 A U-SAXS beamline at the Pohang Accelerator Laboratory. Contact angles were measured using an optical contact angle meter (KRÜSS DSA 100, Germany). The zeta potential was determined using an ELS-1000ZS instrument (Otsuka Electronics). KPFM was performed using a Multimode 8 device (TECSCO). Electrochemical impedance spectroscopy curves were obtained using an electrochemical working station (VMP3, Princeton Applied Research). The open-circuit voltage ( $V_{oc}$ ) and short-circuit current ( $J_{sc}$ ) of the MEGs were measured using a Keithley 6514 electrometer and Keithley 6485 picoammeter. When calculating the current density of the fiber, the surface area of the fiber, when fully extended, is used as the basis for the calculation, in accordance with the power generation principle. RH control was achieved using a humidity chamber comprising a humidifier and humidity sensor in an acrylic case. Experiments at temperatures ranging from 20 to 120 °C were conducted using a heating plate. The flexibility of the fiber-based MEG devices was characterized in three dimensions through rolling, twisting, and bending. For the bending tests, the fiber-based MEG was mounted onto a PET substrate and affixed to a folding apparatus, which aided in examining the MEG performances for different bending angles and fold repetitions.

### Fabrication and testing of self-powered synaptic device

The device exhibited a sandwich-like structure and contained ITO and Ag as the bottom and top electrodes, respectively. At the core of this structure was a 2D chiral perovskite layer, which functioned as the active layer nestled between the two electrodes. The composition of the active layer is particularly notable as it incorporates enantiomers—specifically (R)-(+)- $\alpha$ -methylbenzylamine (R-MBA) and (S)-(–)- $\alpha$ -Methylbenzylamine (S-MBA)—as the organic constituents. These were combined with Pb as the metallic element and a blend of iodide- and bromide-type halides. The resulting active-layer chemical (R/S-(MBA)<sub>2</sub>PbI<sub>4(1-x)</sub>Br<sub>4x</sub>) was integrated into a 4 × 4 crossbar array device. The unit of this device was connected to a fiber-based MEG using gold wire.

### Molecular dynamics simulations

Classical molecular dynamics simulations were conducted to explore the mixed systems at the atomic level. Two distinct bulk systems, designated as PDDA/NaAlg and pure NaAlg, were constructed for these simulations. The PDDA/NaAlg system comprised 100 ALGI, 100 PDDA, 1000 Na, and 2000 Cl molecules, whereas pure NaAlg included 100 ALGI and 1000 Na molecules. Initial configurations for both systems were generated using PACKMOL software<sup>45</sup>.

The partial charge for the target molecules was computed using Gaussian 16 suite with the 6-311g(d,p) basis set<sup>46</sup>. The OPLSAA force field was used to model interactions between ALGI, PDDA, Na, and Cl; this force field encompasses both nonbonded and bonded interactions, with the latter including van der Waals (vdW) and electrostatic components, as expressed using Eqs. (1) and (2), respectively.

$$E_{LJ}(r_{ij}) = 4\epsilon_{ij} \left( \left( \frac{\sigma_{ij}}{r_{ij}} \right)^{12} - \left( \frac{\sigma_{ij}}{r_{ij}} \right)^6 \right), \quad (1)$$

$$E_c(r_{ij}) = \frac{q_i q_j}{4\pi\epsilon_0\epsilon_r r_{ij}}, \quad (2)$$

where  $q_i$  and  $q_j$  represent atomic charges,  $r_{ij}$  is the interatomic distance,  $\sigma$  is the atomic diameter, and  $\epsilon$  denotes the atomic energy parameter. For the diverse atom types, geometric mixing rules were applied to calculate the vdW interactions (Eq. (3)). The cutoff for the vdW and electrostatic interactions was set to 1.2 nm. Long-range electrostatic

interactions were computed using the particle-mesh Ewald method.

$$\sigma_{ij} = \left( \sigma_{ii} * \sigma_{jj} \right)^{\frac{1}{2}}; \epsilon_{ij} = \left( \epsilon_{ii} * \epsilon_{jj} \right)^{\frac{1}{2}}. \quad (3)$$

The simulations commenced with an energy minimization step to relax the system. Subsequently, an isothermal–isobaric (NPT) ensemble with a time step of 1.0 fs was implemented to optimize the simulation box, with the temperature and pressure maintained at 298.15 K and 1.0 atm, respectively. Temperature and pressure were stabilized using the Nosé–Hoover thermostat and the Parrinello–Rahman barostat, respectively. A 10.0 ns NPT optimization period helped attain a stable box size. The atomic motions in all simulations were dictated by classical Newtonian mechanics, which were solved using the velocity Verlet algorithm; these simulations were performed using the GRO-MACS 2021.5 package. Pore size distribution analysis was conducted using Zeo++<sup>47</sup>.

### Density functional theory calculations

The electrostatic potential calculations for NaAlg and PDDA were performed using Gaussian software. For optimization, the PBE/PBE/gen functional was used with the freq 6-31 G + (d,p) basis set, and Grimme's D3 dispersion with Becke–Johnson damping was included (em = gd3bj). The graphical depictions of the molecular structures were meticulously crafted using Visual Molecular Dynamics (VMD) and Multiwfn software<sup>48,49</sup>. An implicit solvation model, the solvation model based on density (SMD), was used to account for solvent effects.

### Data availability

The authors declare that the data supporting the findings of this study are available within the paper and its Supplementary Information files. Source data are provided with this paper.

### References

- Liu, X. et al. Power generation from ambient humidity using protein nanowires. *Nature* **578**, 550 (2020).
- Wang, H. et al. Bilayer of polyelectrolyte films for spontaneous power generation in air up to an integrated 1000 V output. *Nat. Nanotechnol.* **16**, 811 (2021).
- Jiang, W., Lee, S., Zan, G., Zhao, K. & Park, C. Alternating current electroluminescence for human-interactive sensing displays. *Adv. Mater.* **36**, 2304053 (2024).
- Kim, H., Zan, G., Seo, Y., Lee, S. & Park, C. Stimuli-responsive liquid metal hybrids for human-interactive electronics. *Adv. Funct. Mater.* **34**, 2308703 (2023).
- Xu, W. et al. A droplet-based electricity generator with high instantaneous power density. *Nature* **578**, 392 (2020).
- Shi, X. et al. Large-area display textiles integrated with functional systems. *Nature* **591**, 240 (2021).
- Reddy, P., Jang, S., Segalman, R. A. & Majumdar, A. Thermoelectricity in molecular junctions. *Science* **315**, 1568–1571 (2007).
- Kim, G. et al. A deformable complementary moisture and tribo energy harvester. *Energ. Environ. Sci.* **17**, 134–148 (2024).
- Yan, H., Liu, Z. & Qi, R. A review of humidity gradient-based power generator: devices, materials and mechanisms. *Nano Energy* **101**, 107591 (2022).
- Cao, Y., Xu, B., Li, Z. & Fu, H. Advanced design of high-performance moist-electric generators. *Adv. Funct. Mater.* **33**, 2301420 (2023).
- Shao, B. et al. Electricity generation from phase transitions between liquid and gaseous water. *Adv. Energy Mater.* **13**, 2204091 (2023).
- Wang, X. et al. Hydrovoltaic technology: from mechanism to applications. *Chem. Soc. Rev.* **51**, 4902–4927 (2022).
- Wei, Q. et al. Moisture electricity generation: mechanisms, structures, and applications. *Nano Res.* **16**, 7496–7510 (2023).

14. Xu, T., Ding, X., Cheng, H., Han, G. & Qu, L. Moisture-enabled electricity from hygroscopic materials: a new type of clean energy. *Adv. Mater.* **36**, 2209661 (2023).
15. Shen, D. et al. Moisture-enabled electricity generation: from physics and materials to self-powered applications. *Adv. Mater.* **32**, 2003722 (2020).
16. Liu, Z. et al. Recent advances in two-dimensional materials for hydrovoltaic energy technology. *Exploration* **3**, 20220061 (2023).
17. Zhao, F., Cheng, H., Zhang, Z., Jiang, L. & Qu, L. Direct power generation from a graphene oxide film under moisture. *Adv. Mater.* **27**, 4351–4357 (2015).
18. Zhao, F., Liang, Y., Cheng, H., Jiang, L. & Qu, L. Highly efficient moisture-enabled electricity generation from graphene oxide frameworks. *Energ. Environ. Sci.* **9**, 912–916 (2016).
19. Liu, J. et al. Moisture-enabled electricity generation from gradient polyoxometalates-modified sponge-like graphene oxide monolith. *J. Mater. Sci.* **54**, 4831–4841 (2019).
20. Qi, X. et al. Ultralight PEDOT:PSS/graphene oxide composite aerogel sponges for electric power harvesting from thermal fluctuations and moist environment. *Nano Energy* **77**, 105096 (2020).
21. Xiong, C. et al. Carbonized wood cell chamber-reduced graphene oxide@PVA flexible conductive material for supercapacitor, strain sensing and moisture-electric generation applications. *Chem. Eng. J.* **418**, 129518 (2021).
22. Huang, Y., Cheng, H., Shi, G. & Qu, L. Highly efficient moisture-triggered nanogenerator based on graphene quantum dots. *ACS Appl. Mater. Int.* **9**, 38170–38175 (2017).
23. Li, Q. et al. Flexible carbon dots composite paper for electricity generation from water vapor absorption. *J. Mater. Chem. A* **6**, 10639–10643 (2018).
24. Zhang, Y., MohebbiPour, A., Mao, J., Mao, J. & Ni, Y. Lignin reinforced hydrogels with multi-functional sensing and moist-electric generating applications. *Int. J. Biol. Macromol.* **193**, 941–947 (2021).
25. Shin, E. et al. Environmentally sustainable moisture energy harvester with chemically networked cellulose nanofiber. *Energ. Environ. Sci.* **17**, 7165–7181 (2024).
26. Pan, X. et al. An adaptive ionic skin with multiple stimulus responses and moist-electric generation ability. *J. Mater. Chem. A* **8**, 17498–17506 (2020).
27. Li, S. et al. A biodegradable silk-based energy-generating skin with dual-mode tactile perception. *Device*, <https://doi.org/10.1016/j.device.2024.100561>.
28. Liu, J. et al. Moisture-enabled hydrovoltaic power generation with milk protein nanofibrils. *Nano Energy* **102**, 107709 (2022).
29. Wang, L. et al. Flexible, self-cleaning, and high-performance ceramic nanofiber-based moist-electric generator enabled by interfacial engineering. *Sci. China Technol. Sc.* **65**, 450–457 (2022).
30. Zhao, K. et al. Humidity-Tolerant Moisture-driven energy generator with mxene aerogel-organohydrogel Bilayer. *ACS Nano* **17**, 5472–5485 (2023).
31. Xu, T. et al. An efficient polymer moist-electric generator. *Energ. Environ. Sci.* **12**, 972–978 (2019).
32. Bai, J. et al. Sunlight-coordinated high-performance moisture power in natural conditions. *Adv. Mater.* **34**, 2103897 (2022).
33. He, W. et al. Textile-based moisture power generator with dual asymmetric structure and high flexibility for wearable applications. *Nano Energy* **95**, 107017 (2022).
34. Wang, H. et al. Transparent, self-healing, arbitrary tailorable moist-electric film generator. *Nano Energy* **67**, 104238 (2020).
35. Bediako, J. K. et al. Saloplastics and the polyelectrolyte complex continuum: advances, challenges and prospects. *Chem. Eng. J.* **462**, 142322 (2023).
36. Fu, J. & Schlenoff, J. B. Driving forces for oppositely charged polyion association in aqueous solutions: enthalpic, entropic, but not electrostatic. *J. Am. Chem. Soc.* **138**, 980–990 (2016).
37. Chen, S., Guo, Q. & Yu, J. Bio-inspired functional coacervates. *Aggregate* **3**, e293 (2022).
38. Sun, Z. et al. Weavable yarn-shaped moisture-induced electric generator. *Nano Energy* **116**, 108748 (2023).
39. Liang, Y. et al. Self-powered wearable graphene fiber for information expression. *Nano Energy* **32**, 329–335 (2017).
40. Shao, C. et al. Wearable fiberform hygroelectric generator. *Nano Energy* **53**, 698–705 (2018).
41. Wang, Z. et al. Unipolar solution flow in calcium-organic frameworks for seawater-evaporation-induced electricity generation. *J. Am. Chem. Soc.* **146**, 1690–1700 (2024).
42. Victoria Traffano-Schiffo, M., Castro-Giraldez, M., Fito, P. J., Perullini, M. & Santagapita, P. R. Gums induced microstructure stability in Ca(II)-alginate beads containing lactase analyzed by SAXS. *Carbohydr. Polym.* **179**, 402–407 (2018).
43. Li, X. et al. Superstrong ionogel enabled by coacervation-induced nanofibril assembly for sustainable moisture energy harvesting. *ACS Nano*, **18**, 12970–12980 (2024).
44. Liu, C. et al. Unveil the triple roles of water molecule on power generation of mxene derived TiO<sub>2</sub> based moisture electric generator. *Adv. Energy Mater.* **14**, 2400590 (2024).
45. Martinez, L., Andrade, R., Birgin, E. G. & Martinez, J. M. PACKMOL: a Package for building initial configurations for molecular dynamics simulations. *J. Comput. Chem.* **30**, 2157–2164 (2009).
46. Petersson, G. A. & Allaham, M. A. A complete basis set model chemistry 2. Open-shell systems and the total energies of the 1st-row atoms. *J. Chem. Phys.* **94**, 6081–6090 (1991).
47. Willems, T. F., Rycroft, C., Kazi, M., Meza, J. C. & Haranczyk, M. Algorithms and tools for high-throughput geometry-based analysis of crystalline porous materials. *Microporous Mesoporous Mater.* **149**, 134–141 (2012).
48. Lu, T. & Chen, F. Multiwfn: a multifunctional wavefunction analyzer. *J. Comput. Chem.* **33**, 580–592 (2012).
49. Humphrey, W., Dalke, A. & Schulten, K. VMD: visual molecular dynamics. *J. Mol. Graph. Model.* **14**, 33–38 (1996).

## Acknowledgements

This research was supported by the National Research Foundation of Korea (NRF), funded by the Korean Government (MEST) (RS-2023-00208577 to C.P.), the Nano & Material Technology Development Program through the National Research Foundation of Korea (NRF), funded by Ministry of Science and ICT (RS-2024-00451891 and RS-2024-00416938 to C.P.), the Creative Materials Discovery Program and the Pioneer Research Center Program through the National Research Foundation of Korea (NRF), funded by the Ministry of Science, ICT & Future Planning (2022M3C1A3Q81211 to C.P.), and the Open Resource Research Program of the Korea Institute of Science and Technology (2E32961 to C.P.).

## Author contributions

C.P. conceived and led the study; G.Z., W.J., H.K., K.Z., and S.L. designed and carried out the experiments; G.Z. and K.L. contributed to simulations; J.J., G.K., E.S., W.K., Y.K., J.W.P., J.S., and H.K. contributed to materials characterization and data analysis; J.W.O. and J.O. designed the moisture control setup; T.K. and S.L. collected SAXS data; G.Z. drafted the paper with all authors providing feedback.

## Competing interests

The authors declare no competing interests.

## Additional information

**Supplementary information** The online version contains supplementary material available at <https://doi.org/10.1038/s41467-024-54442-4>.

**Correspondence** and requests for materials should be addressed to Cheolmin Park.

**Peer review information** *Nature Communications* thanks Weigang Ma, Xi YAO, and the other, anonymous, reviewer(s) for their contribution to the peer review of this work. A peer review file is available.

**Reprints and permissions information** is available at <http://www.nature.com/reprints>

**Publisher's note** Springer Nature remains neutral with regard to jurisdictional claims in published maps and institutional affiliations.

**Open Access** This article is licensed under a Creative Commons Attribution-NonCommercial-NoDerivatives 4.0 International License, which permits any non-commercial use, sharing, distribution and reproduction in any medium or format, as long as you give appropriate credit to the original author(s) and the source, provide a link to the Creative Commons licence, and indicate if you modified the licensed material. You do not have permission under this licence to share adapted material derived from this article or parts of it. The images or other third party material in this article are included in the article's Creative Commons licence, unless indicated otherwise in a credit line to the material. If material is not included in the article's Creative Commons licence and your intended use is not permitted by statutory regulation or exceeds the permitted use, you will need to obtain permission directly from the copyright holder. To view a copy of this licence, visit <http://creativecommons.org/licenses/by-nc-nd/4.0/>.

© The Author(s) 2024